Puncture black hole initial data: A single domain Galerkin-collocation method for trumpet and wormhole data sets

P. C. M. Clemente and H. P. de Oliveira[*]

Departamento de Física Teórica—Instituto de Física A. D. Tavares,
Universidade do Estado do Rio de Janeiro R. São Francisco Xavier,
524. Rio de Janeiro, Rio de Janeiro 20550-013, Brazil

We present a single-domain Galerkin-collocation method to calculate puncture initial data sets for single and binary black holes, either in the trumpet or wormhole geometries. The combination of aspects belonging to the Galerkin and the collocation methods together with the adoption of spherical coordinates in all cases are shown to be very effective. We propose a unified expression for the conformal factor to describe trumpet and spinning black holes. In particular, for the spinning trumpet black holes, we exhibit the deformation of the limit surface due to the spin from a sphere to an oblate spheroid. We also revisit the energy content in the trumpet and wormhole puncture data sets. The algorithm can be extended to describe binary black holes.

I. INTRODUCTION

The precise characterization of the gravitational and matter fields on some spatial hypersurface constitutes the initial data problem in numerical relativity [1]. In this instance, it is possible to identify if there exist interacting black holes and neutrons stars together (or not) with any other distribution of matter, which offers an ideal setup to simulate astrophysical situations in which the high gravitational field plays a central role. In parallel to the decades-long effort to directly detect gravitational radiation (which has been accomplished recently [2]), there has also been an endeavor to predict gravitational-wave signals from compact binaries using numerical simulations. These simulations [3–5] start with initial data in general containing binary black holes.

In more precise terms, the initial data problem in general relativity consists in specifying the spatial metric and extrinsic curvature, γ_{ij} and K_{ij}, respectively, on a given spatial hypersurface. These quantities must satisfy the Hamiltonian and momentum constraint equations of the Cauchy formulation of the field equations [6]. The most important strategy for solving the constrained equations is to introduce a conformal transformation of the spatial metric to a known background metric, $\bar{\gamma}_{ij}$, and a similar transformation involving the extrinsic curvature [7]. Then,

$$\gamma_{ij} = \Psi^4 \bar{\gamma}_{ij}, \tag{1}$$

$$A_{ij} = \Psi^{-2} \bar{A}_{ij}, \tag{2}$$

where Ψ is the conformal factor and A_{ij} is the traceless part of the extrinsic curvature such that

$$K_{ij} = A_{ij} + \frac{1}{3}\gamma_{ij}K, \tag{3}$$

with K being the trace of K_{ij}. In this formulation, the set of functions $(\Psi, \bar{\gamma}_{ij}, \bar{A}_{ij}, K)$ specified in the initial hypersurface characterizes the initial data. These quantities are not fixed by the constraint equations but must satisfy them. We have adopted here the Bowen-York solution [8] for the extrinsic curvature obtained with the requirements of conformal flatness, maximal slicing, $K = 0$, and vacuum. In this case, it is possible to decouple the Hamiltonian and momentum constraints which, respectively, become

$$\bar{\nabla}^2 \Psi + \frac{1}{8}\Psi^{-7}\bar{A}^{ij}\bar{A}_{ij} = 0, \tag{4}$$

$$\bar{D}_i \bar{A}^{ij} = 0, \tag{5}$$

where $\bar{D}_i = \bar{\gamma}_{ij}\nabla^j$ is the covariant derivative associated with the flat background metric $\bar{\gamma}_{ij}$ and $\bar{\nabla}^2$ is the flat-space Laplacian operator. Remarkably, Eq. (5) can be solved analytically to describe boosted and spinning black holes denoted by $\bar{A}_{\mathbf{P}}^{ij}$ and $\bar{A}_{\mathbf{S}}^{ij}$, whose corresponding expressions are

$$\bar{A}_{\mathbf{P}}^{ij} = \frac{3}{2r^2}[2P^{(i}n^{j)} - (\eta^{ij} - n^i n^j)\mathbf{n}.\mathbf{P}], \tag{6}$$

$$\bar{A}_{\mathbf{S}}^{ij} = \frac{6}{r^3}n^{(i}\epsilon_{mp}^{j)}J^m n^p, \tag{7}$$

where $\mathbf{P}$ and $\mathbf{J}$ are, respectively, the Arnowitt-Deser-Misner (ADM) linear and angular momenta carried by the black hole [9]. The quantity $n^k = x^k/r$ is the normal vector pointing

---

[*]hp.deoliveira@pq.cnpq.br

away from the black hole located at $r = 0$. Due to the linearity of the momentum constraint, we can construct spacetimes containing a boosted spinning black hole or multiple black holes by superposing the corresponding expressions for the conformal extrinsic curvatures given by Eqs. (6) and (7).

In general, the Hamiltonian constraint (4) is solved numerically for the conformal factor after specifying the extrinsic curvature $\bar{A}_{ij}$. To guarantee that there are black holes in the initial hypersurface it is necessary to satisfy appropriate boundary conditions which are dictated by the excision or puncture methods. We are going to focus here on the puncture method that consists [10] in decomposing the conformal factor into two pieces: the background component containing the black hole singularities which are given analytically, and the regular component which is obtained by solving the Hamiltonian constraint numerically. Accordingly, we have

$$\Psi = \Psi_0 + u. \qquad (8)$$

Considering a single black hole, Ψ_0 is taken as the Schwarzschild black hole in its wormhole representation, or equivalently on a slice of constant Schwarzschild time. It means that

$$\Psi_0 = 1 + \frac{m_0}{2r}, \qquad (9)$$

where $r = 0$ locates the puncture and m_0 is a free parameter. It can be verified that the above expression is the solution of the Hamiltonian constraint for $\bar{A}_{ij} = 0$ and $u = 0$, and in this situation the parameter m_0 is the ADM mass. The substitution of Eqs. (8) and (9) into the Hamiltonian constraint (4) results in an elliptic equation for the regular component u. We can construct initial data with multiple black holes by a direct generalization of the background conformal factor to $\Psi_0 = 1 + \sum_k m_k/2r_k$, where each puncture m_k is located at $r_k = 0$. Of particular interest is the case of binary black holes, for which most of the initial data used in the simulations adopt the puncture method [4,11–16].

There is another representation of the Schwarzschild black hole based on spatial slices that terminate at nonzero areal radius known as the trumpet representation. The interest in constructing trumpet initial data has increased after the advent of the moving puncture method [4,5]. It has been shown that the Schwarzschild wormhole puncture data evolves in such a way that the numerical slices tend to a spatial slice with finite areal radius or trumpets [17–20]. Therefore, it is motivating to construct initial trumpet data for single and binary black holes endowed with spin and linear momentum. In this direction, we mention the derivation of the analytical solutions for maximally sliced and $1 + \log$ trumpet Schwarzschild black holes in Refs. [21,22], respectively. The initial data for single (spinning and boosted) and

binary trumpets were studied by Hannan *et al.* [23], and Immerman and Baumgarte [24]. More recently, Dietrich and Brugman [26] constructed $1 + \log$ sliced initial data for single and binary systems.

We present here a single-domain algorithm based on the Galerkin-collocation spectral method [27–29] to obtain wormhole and trumpet initial data sets. The algorithm is distinct from other spectral codes [30–33], but nonetheless it is very efficient and simple. We believe that this task is valuable in its own right. The selection of the radial and angular basis functions is of crucial importance; we chose the spherical harmonics since they are the most natural basis functions for the angular domain in general, whereas the radial basis functions are expressed as appropriate linear combinations of the Chebyshev polynomials to satisfy the boundary conditions. The algorithm is well suited to describe a spinning and boosted single black hole, a wormhole, or a trumpet binary system.

The paper is divided as follows. After the Introduction in Sec. I, we present the basic equations for constructing trumpet initial data sets. We use the maximal sliced analytical solution of Naculich and Baumgarte [21] to establish a convenient expression for the conformal factor describing single or binary trumpets. The numerical scheme is detailed in Sec. III. We present the numerical tests and discuss some cases of interest in Sec. IV. In particular, we highlight the proposed unified description of a single trumpet spinning and a trumpet black hole. For a single spinning black hole, we show the influence of the spin in altering the minimal surface from a sphere to an oblate spheroid. As the last application involving a single black hole, we revisit the amount of junk radiation present in the spinning and boosted trumpet/wormhole black holes. We also consider wormhole and trumpet binaries to illustrate the feasibility of the algorithm in more general cases. Finally, in Sec. V we conclude and describe some possible extensions of the present investigation.

II. TRUMPET AND WORMHOLE PUNCTURE DATA SETS

The starting point to construct maximal sliced puncture trumpet initial data is to establish the trumpet slicing of the Schwarzschild spacetime. Baumgarte and Naculich [21] have derived the corresponding exact conformal factor as a function of the areal radius $R = r\Psi_0^2$ (cf. Appendix A). With the exact solution, they have shown the following asymptotic behavior:

$$\Psi_0 = \left(\frac{3m_0}{2r}\right)^{1/2}, \qquad r \to 0, \qquad (10)$$

$$\Psi_0 = 1 + \frac{m_0}{2r}, \qquad r \to \infty, \qquad (11)$$

where m_0 is the Schwarzschild mass. The corresponding expression for the traceless part of the extrinsic curvature is

$$\bar{A}_0^{ij} = \frac{3\sqrt{3}m_0^2}{4r^3}(\bar{\gamma}^{ij} - 3n^i n^j). \tag{12}$$

In the case of wormhole data we have $\bar{A}_0^{ij} = 0$. With the above expression it can be shown that the momentum constraint $\bar{D}_i \bar{A}_0^{ij} = 0$ is satisfied along with the validity of the Hamiltonian constraint,

$$\bar{\nabla}^2 \Psi_0 + \frac{1}{8}\Psi_0^{-7}\bar{A}_0^{ij}\bar{A}_{ij}^0 = 0, \tag{13}$$

where

$$\bar{A}_0^{ij}\bar{A}_{ij}^0 = \frac{81m_0^4}{8r^6}. \tag{14}$$

For the trumpet initial data sets, we propose the following puncture-like expression for the conformal factor:

$$\Psi = \Psi_0(1+u), \tag{15}$$

where Ψ_0 is the trumpet Schwarzschild solution. Introducing the new conformal factor into the Hamiltonian constraint (4), we obtain

$$\bar{\nabla}^2 u + \frac{2\bar{D}_i\Psi_0\bar{D}^i u}{\Psi_0} + \frac{\bar{A}^{ij}\bar{A}_{ij}}{8\Psi_0^8(1+u)^7} - \frac{(1+u)}{8\Psi_0^8}\bar{A}_0^{ij}\bar{A}_{ij}^0 = 0, \tag{16}$$

where the total traceless part of the extrinsic curvature is given by

$$\bar{A}^{ij} = \bar{A}_0^{ij} + \bar{A}_{\mathbf{P}}^{ij} + \bar{A}_{\mathbf{S}}^{ij} \tag{17}$$

due to the linearity of the momentum constraint equation. In the case of the wormhole data sets the conformal factor is expressed by Eq. (8) and the Hamiltonian equation becomes

$$\bar{\nabla}^2 u + \frac{1}{8}(\Psi_0 + u)^{-7}\bar{A}^{ij}\bar{A}_{ij} = 0, \tag{18}$$

with $\bar{A}_0^{ij} = 0$ and Ψ_0 given by Eq. (9).

The main reason for not adopting the usual decomposition for the conformal factor [Eq. (8)] for trumpet black hole data sets is to provide a unified framework for describing spinning and boosted black holes with regular functions u. For instance, for a single trumpet spinning black hole in which $\Psi = \Psi_0 + u$, it can be shown that [23,24] $u \sim \mathcal{O}(r^{-1/2})$ near $r = 0$, and for a single boosted black hole $u \sim \mathcal{O}(r)$. On the other hand, by considering the puncture-like expression (15), we follow the analysis of Immerman and Baumgarte [24] of the behavior of u near

the puncture at $r = 0$ for a boosted (u_P) and a spinning black hole (u_S) in the axisymmetric case. Assuming that $u \ll 1$, the corresponding Hamiltonian constraints are approximated by

$$\bar{\nabla}^2 u_P - \frac{1}{r}\frac{\partial u_P}{\partial r} \approx \frac{\sqrt{3}P\cos\theta}{3m_0^2 r} + 2\frac{u_P}{r^2}, \tag{19}$$

$$\bar{\nabla}^2 u_S - \frac{1}{r}\frac{\partial u_S}{\partial r} \approx -\frac{4J^2\sin^2\theta}{9m_0^4 r^2} + \left(1 + \frac{28J^2\sin^2\theta}{9m_0^4}\right)\frac{u_S}{r^2}. \tag{20}$$

From these equations one can show that near the origin

$$u_P \sim \mathcal{O}(r), \quad \text{and} \quad u_S \sim \mathcal{O}(1). \tag{21}$$

The above behaviors near the origin can be dealt with numerically without difficulties.

To guarantee that the spacetime is asymptotically flat, the function u must satisfy the following asymptotic condition:

$$u = \frac{\delta m}{r} + \mathcal{O}(r^{-2}), \tag{22}$$

where $\delta m = \delta m(\theta, \phi)$ in general after adopting the spherical coordinates. As indicated in the sequence, the function δm is the contribution due to angular and linear momenta to the ADM mass which is calculated from

$$M_{\text{ADM}} = -\frac{1}{2\pi}\lim_{r\to\infty}\int_\Omega r^2\Psi_{,r}d\Omega. \tag{23}$$

Assuming that the conformal factor is expressed by either Eq. (8) or Eq. (15), and taking into account the behavior of u and Ψ_0 for $r \to \infty$, we obtain

$$M_{\text{ADM}} = m_0 + \frac{1}{2\pi}\int_0^{2\pi}\int_0^\pi \delta m(\theta, \phi)\sin\theta d\theta d\phi. \tag{24}$$

According to the numerical scheme of the next section, we can obtain an analytical expression for $\delta m(\theta, \phi)$, and the ADM mass is calculated straightforwardly. In the case of multiple black holes, we have to replace $m_0 \to \sum m_i$ in the above expression.

III. THE GALERKIN-COLLOCATION ALGORITHM

We present here the Galerkin-collocation scheme to solve the Hamiltonian constraint (16) or (18) for trumpet and wormhole data sets. The centerpiece of the numerical treatment is the spectral approximation of the function $u(r, \theta, \phi)$ given by

$$u_a(r,\theta,\phi) = \sum_{k,l=0}^{N_x,N_y} \sum_{m=-l}^{l} c_{klm}\chi_k(r)Y_{lm}(\theta,\phi). \quad (25)$$

Here c_{klm} represents the unknown coefficients or modes, and N_x and N_y are, respectively, the radial and angular truncation orders that limit the number of terms in the above expansion. The angular patch has the spherical harmonics $Y_{lm}(\theta,\phi)$ as the basis functions. The choice of spherical coordinates together with the adoption of spherical harmonics as the angular basis functions are quite natural and (as we are going to show) computationally very efficient. Concerning the radial basis functions $\chi_k(r)$, we have followed the prescription of the Galerkin method in which each basis function satisfies the boundary conditions. Usually, this is done by establishing an appropriate combination of Chebyshev polynomials. Near $r = 0$, we have

$$\chi_k(r) \sim \mathcal{O}(r) \quad \text{and} \quad \chi_k(r) \sim \mathcal{O}(1) \quad (26)$$

according to the boundary conditions (21). The asymptotic behavior of each basis function is

$$\chi_k(r) \sim \mathcal{O}(r^{-1}). \quad (27)$$

To satisfy these boundary conditions, we define each radial basis function as

$$\chi_k(r) = \frac{1}{2}(TL_{k+2}(r) - TL_k(r)), \quad (28)$$

$$\chi_k(r) = \frac{1}{2}(TL_{k+1}(r) - TL_k(r)) \quad (29)$$

for boosted and spinning black holes, respectively. For the wormhole case the basis function is given by Eq. (29). Here $TL_k(r)$ represents the rational Chebyshev polynomials defined by

$$TL_k(r) = T_k\left(x = \frac{r - L_0}{r + L_0}\right), \quad (30)$$

where $T_k(x)$ is the Chebyshev polynomial of kth order and L_0 is the map parameter that connects $-1 \leq x < 1$ to $0 \leq r < \infty$ through the algebraic map [25] $r = L_0(1 + x)/(1 - x)$.

The spherical harmonics are in general complex functions. Therefore, the coefficients c_{klm} must be complex but also satisfy some symmetry conditions to guarantee that the conformal factor is a real function. The symmetry conditions are

$$c^*_{kl-m} = (-1)^{-m}c_{klm} \quad (31)$$

due to the symmetry relation of the spherical harmonics $Y^*_{l-m}(\theta,\phi) = (-1)^{-m}Y_{lm}(\theta,\phi)$. Consequently, the number of independent modes is $(N_x + 1)(N_y + 1)^2$.

We now establish the residual equation associated with the Hamiltonian constraint by substituting the spectral approximation (25) for the function u into the Hamiltonian constraint (16) [or (18)]. In addition, we have taken into account the differential equation for the spherical harmonics to get rid of those terms involving derivatives with respect to θ and ϕ. After a straightforward calculation, we arrive at the following expression:

$$\begin{aligned}
\mathrm{Res}(r,\theta,\phi) = &\sum_{k,n,p} c_{knp}\left[\frac{1}{r^2}\frac{\partial}{\partial r}\left(r^2\frac{\partial\chi_k}{\partial r}\right) - \frac{n(n+1)}{r^2}\chi_k\right] \\
&\times Y_{np}(\theta,\phi) + \frac{2}{\Psi_0}\frac{\partial\Psi_0}{\partial R}\frac{\partial R}{\partial r}\frac{\partial u_a}{\partial r} \\
&- \frac{(1 + u_a(r,\theta,\phi))}{8\Psi_0^8}(\bar{A}^{ij}\bar{A}_{ij})_0 \\
&+ \frac{(1 + u_a(r,\theta,\phi))^{-7}}{8\Psi_0^8}\bar{A}^{ij}\bar{A}_{ij}. \quad (32)
\end{aligned}$$

In the case of binary systems with trumpet punctures, it is necessary to modify the second term on the rhs to include the angular dependence that appears in the background solution Ψ_0.

The next and final step is to describe the procedure to obtain the coefficients c_{klm}. From the method of weighted residuals [34], these coefficients are evaluated with the condition that the residual equation is forced to zero in an average sense. This means that

$$\begin{aligned}
&\langle \mathrm{Res}, R_j(r)S_{lm}(\theta,\phi)\rangle \\
&= \int_{\mathcal{D}} \mathrm{Res}R_j^*(r)S_{lm}^*(\theta,\phi)w_rw_\theta w_\phi r^2drd\Omega = 0, \quad (33)
\end{aligned}$$

where the functions $R_j(r)$ and $S_{lm}(\theta,\phi)$ are called the test functions, while w_r, w_θ, and w_ϕ are the corresponding weights. We have chosen the radial test function as prescribed by the collocation method,

$$R_j(r) = \delta(r - r_j), \quad (34)$$

which is the Dirac delta function; r_j represents the radial collocation points and $w_r = 1$. Following the Galerkin method we identify the angular test function $S_{lm}(\theta,\phi)$ as the spherical harmonics, and consequently $w_\theta = w_\phi = 1$. Therefore, Eq. (33) becomes

$$\langle \mathrm{Res}(r,\theta,\phi), Y_{lm}(\theta,\phi)\rangle_{r=r_j} = 0, \quad (35)$$

where $j = 0, 1, .., N_x$, $l = 0, 1, .., N_y$, and $m = 0, 1, .., l$. The $N_x + 1$ radial collocation points are

$$r_j = \frac{L_0(1 + \tilde{x}_j)}{1 - \tilde{x}_j}, \quad (36)$$
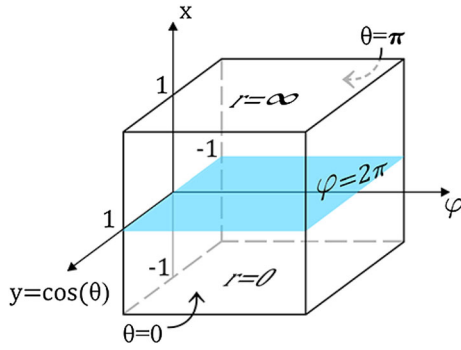
FIG. 1. The three-dimensional spatial domain viewed as a cube described by the coordinates $-1 \leq x < 1$, $-1 < y < 1$ ($y = \cos\theta$) that correspond to $0 \leq r < \infty$ and $0 \leq \theta \leq \pi$, while the azimuthal angle ϕ is maintained.

with the Chebyshev-Gauss collocation points $\tilde{x}_j$ in the computational domain,

$$\tilde{x}_j = \cos\left[\frac{(2j+1)\pi}{2N_x+2}\right], \qquad j = 0, 1, .., N_x. \quad (37)$$

We have excluded the point at infinity ($\tilde{x} = 1$) since the residual equation (32) is identically satisfied asymptotically due to the choice of the radial basis functions. Notice that the origin is also excluded. In Fig. 1 we show schematically the spatial domain spanned by the new coordinates ($\tilde{x}, y = \cos\theta, \phi$).

We are in a position to schematically present the set of equations resulting from the relations (35). The integration on the angular domain takes into account the orthogonality of the spherical harmonics in the first three terms of the residual equation (32), whose result is

$$\langle \text{Res}, Y_{lm}(\theta, \phi) \rangle_{r_j}$$
$$= \sum_k c_{klm} \left[\frac{1}{r^2}\frac{\partial}{\partial r}\left(r^2 \frac{\partial \chi_k}{\partial r}\right) - \frac{l(l+1)\chi_k}{r^2}\right]_{r_j}$$
$$+ \left(\frac{2}{\Psi_0}\frac{\partial \Psi_0}{\partial R}\frac{\partial R}{\partial r}\right)_{r_j} \sum_k c_{klm}\left(\frac{\partial \chi_k}{\partial r}\right)_{r_j}$$
$$- \left(\frac{(\bar{A}^{ij}\bar{A}_{ij})_0}{8\Psi_0^8}\right)_{r_j}\left(2\sqrt{\pi}\delta_{0l}\delta_{0m} + \sum_k c_{klm}\chi_k(r_j)\right)$$
$$+ \left\langle \frac{(\bar{A}^{ij}\bar{A}_{ij})}{8\Psi_0^8(1+u_a)^7}, Y_{lm}(\theta, \phi)\right\rangle_{r_j} = 0, \quad (38)$$

with $j = 0, 1, .., N_x$, $l = 0, 1, .., N_y$, and $m = -l, .., l$. The last term is calculated using quadrature formulas as indicated below:

$$\langle (..), Y_{lm}(\theta, \phi) \rangle_{r_j} \approx \sum_{k,n=0}^{N_1,N_2} (..) Y_{lm}^*(\theta_k, \phi_n) v_k^\theta v_n^\phi, \quad (39)$$

where (θ_k, ϕ_n), $k = 0, 1, .., N_1$, $n = 0, 1, .., N_2$ are the quadrature collocation points, and $v_k^\theta v_n^\phi$ are the corresponding weights [35]. To achieve better accuracy we have set $N_1 = N_2 = 2N_y + 1$, but this is not mandatory since it is possible to use simply $N_1 = N_2 = N_y$. In summary, we have to solve a set of $(N_x + 1)(N_y + 1)^2$ nonlinear algebraic equations indicated by Eq. (38) for an equal number of coefficients c_{klm}. For this aim, the Newton-Raphson algorithm is employed. We originally implemented the computational procedure indicated in this section in MAPLE, as well as a faster version in PYTHON.

IV. APPLICATIONS

A. Single spinning and boosted black holes

We begin by considering a single spinning or boosted black hole located at the origin $r = 0$. In each case the angular and linear momenta lie on the z axis, that is, $\mathbf{J} = (0, 0, J_0)$ and $\mathbf{P} = (0, 0, P_0)$. The quantities $A_{ij}A^{ij}$ corresponding to spinning and boosted black holes are given by

$$\bar{A}_{ij}\bar{A}^{ij} = \frac{18J_0^2}{r^6}\sin^2\theta + \frac{81m_0^4}{8r^6}, \quad (40)$$

$$\bar{A}_{ij}\bar{A}^{ij} = \frac{9P_0^2}{2r^4}(1 + 2\cos^2\theta) + \frac{81m_0^4}{8r^6} - \frac{27\sqrt{3}m_0^2 P_0}{2r^5}\cos\theta. \quad (41)$$

The resulting Hamiltonian constraint in each case is axisymmetric due to the absence of any dependence on the polar angle ϕ. Thus, in the spectral approximation of the function $u(r, \theta)$ [cf. Eq. (25)] the spherical harmonics are replaced by Legendre polynomials as the angular basis functions.

We have adopted the convergence of the ADM mass evaluated according to Eq. (24) as the main numerical test. From the spectral approximation (25) we can obtain $\delta m(\theta)$ after $-\lim_{r\to\infty} r^2 \partial u_a(r, \theta)/\partial r$ without approximating the infinity to some finite radius r_{max}. We have established the convergence of the ADM mass by calculating the difference of the ADM mass corresponding to approximate solutions with fixed $N_y = 12$ and varying $N_x = 5, 10, 15, \ldots$ such that $\delta M(N_x) = |M_{\text{ADM}}(N_x + 5) - M_{\text{ADM}}(N_x)|$. As reported previously [29], the value of the map parameter can improve the convergence of δM. Figures 2 and 3 show the convergence tests for spinning and boosted black holes, respectively, where in both cases $m_0 = 1.0$; the spin parameter is $J_0 = 0.5m_0^2$ while the boost is $P_0 = 1.0m_0$. In Fig. 2 the results are displayed for $L_0 = 2.0$ and $L_0 = 0.2$ for the trumpet data sets to illustrate the role of L_0 in the convergence rate. Notice that the improvement of the convergence rate is achieved when $L_0 = 0.2$. For the spinning wormhole, the best map parameter is $L_0 = 0.5$, and the convergence is better than in the trumpet case. Figure 3 shows the
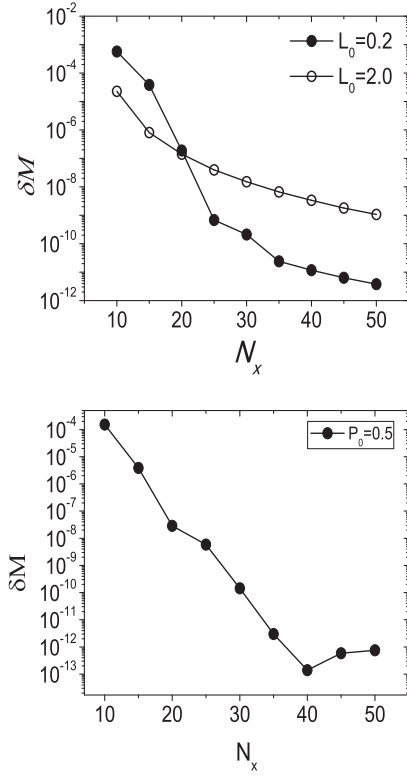
FIG. 2.   Convergence of the ADM mass for trumpet and wormhole spinning punctures (upper and lower graphs, respectively). Here $J_0 = 0.5m_0^2$ and $m_0 = 1.0$. For the trumpet data, we have included two convergence tests corresponding to $L_0 = 0.2$ and $L_0 = 2.0$ to make clear the influence of the map parameter. The exponential convergence of the ADM mass is more evident for $L_0 = 0.2$ than for $L_0 = 2.0$; the convergence is algebraic. For the wormhole spinning puncture the convergence is clearly exponential where $L_0 = 0.5$.

convergence of the ADM mass for trumpet and wormhole boosted black holes with their respective best map parameters, $L_0 = 0.1$ and $L_0 = 2.0$.

Spinning trumpet black holes alter the geometry of the minimal surface characterized by $r = 0$ from a sphere to an oblate spheroid. It will be instructive to quantify this change by evaluating the eccentricity of the spheroid as a function of the spin parameter J_0. The eccentricity of the minimal surface is defined by

$$\epsilon = \sqrt{1 - \frac{R_{\min}^2(J_0, \theta = 0)}{R_{\min}^2(J_0, \theta = \pi/2)}}, \qquad (42)$$

where $R_{\min}(J_0, \theta) = \lim_{r \to 0} r\Psi_0^2(1+u)^2$. We have expressed the eccentricity as a function of J_0/m_0^2 and J_0/M_{ADM}^2 in Fig. 4. Notice that the eccentricity tends to a limit value of $\epsilon \approx 0.439$. We have included an inset plot with the eccentricity calculated from the approximate solution due to Immerman and Baumgarte [24] (continuous line) valid for small J_0 and the corresponding numerical
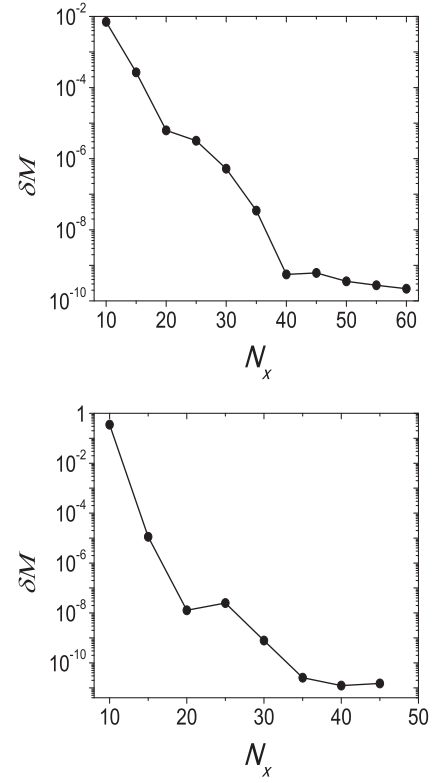
FIG. 3.   Convergence of the ADM mass for trumpet and wormhole boosted punctures (upper and lower graphs, respectively). Here $P_0 = 1.0m_0$ and $m_0 = 1.0$, and the map parameters are $L_0 = 0.1$ and $L_0 = 1.0$, respectively. The exponential convergence is achieved in both cases.

eccentricities (circles). As expected, the disagreement between both results becomes evident as the spin increases.

We revisit the estimate of the radiation content or the junk radiation present in the trumpet and wormhole initial data sets, which have been considered in Refs. [23,36,37]. The radiation content E_{rad} is estimated as [23]

$$E_{\mathrm{rad}} = \sqrt{M_{\mathrm{ADM}}^2 - P^2} - M_{\mathrm{BH}}, \qquad (43)$$

where $P^2 = P_i P^i$, and M_{BH} is the total mass of a black hole evaluated according to the Christodoulou [38] formula

$$M_{\mathrm{BH}}^2 = M_{\mathrm{irr}}^2 + \frac{J^2}{4M_{\mathrm{irr}}^2}, \qquad (44)$$

where $J^2 = J_i J^i$, and M_{irr} is the irreducible mass calculated from

$$M_{\mathrm{irr}} = \sqrt{\frac{A}{16\pi}}, \qquad (45)$$

with A being the area of the apparent horizon. After solving the apparent horizon equation for spinning and boosted black holes (see Appendix B), A can be calculated,
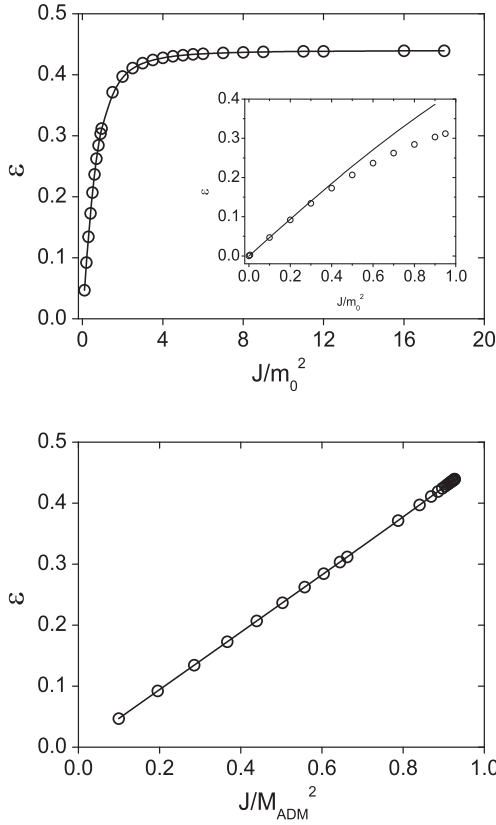
FIG. 4. Both graphs show the eccentricity of the minimal surface versus J_0/m_0^2 and J_0/M_{ADM}^2, respectively. The eccentricity tends to a limit value of about 0.439. In the inset the continuous line represents the approximate exact solution of Ref. [24] valid for small angular momentum parameter together with the numerical eccentricities.

allowing to determine the ratio $e_{rad} \equiv E_{rad}/M_{BH}$ as a function of J_0/M_{BH}^2 and P_0/M_{BH}, respectively. We notice that for spinning black holes the radiation content in the trumpet and wormhole data is nearly the same. However, there is a slight exception for small J_0/M_{BH}^2 in which $(e_{rad})_{trumpet} > (e_{rad})_{wormhole}$ (cf. Fig. 5). On the other hand, the amount of radiation in the trumpet and wormhole boosted black holes is indistinguishable according to Fig. 5.

To illustrate an application of the Galerkin-collocation algorithm to a simple three-dimensional case, we consider a trumpet puncture located at the origin and with linear and intrinsic angular momenta characterized, respectively, by $\mathbf{P} = (P_0, 0, 0)$ and $\mathbf{S} = (0, 0, J_0)$. In this case,

$$\bar{A}_{ij}\bar{A}^{ij} = \frac{18J_0^2}{r^6}\sin^2\theta + \frac{9P_0^2}{2r^4}\left(1 + 2\sin^2\theta\cos^2\phi\right)$$
$$+ \frac{81m_0^4}{8r^6} - \frac{18J_0P_0}{r^5}\sin\theta\sin\phi$$
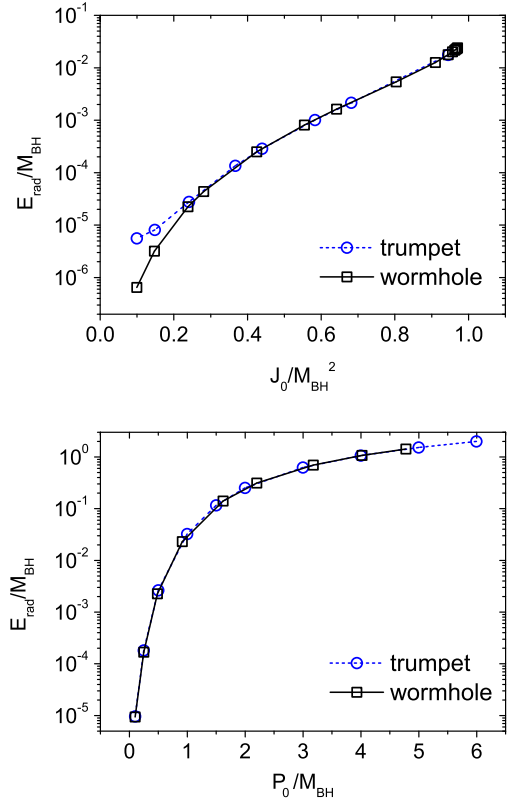$$- \frac{27\sqrt{3}P_0m_0^2}{2r^5}\sin\theta\cos\phi. \tag{46}$$

FIG. 5. Radiation content for spinning and boosted black holes (upper and lower graphs, respectively). The circles and boxes refer to trumpet and wormhole data sets, respectively.

We have adopted the conformal factor as given by Eq. (15) due to the presence of spin, and the relevant parameters are $m_0 = 1$, $P_0 = 0.2m_0$, and the spin parameter assumes several values, $J_0 = 0.1m_0^2, 0.2m_0^2, .., 0.5m_0^2$. The influence of increasing the spin parameter on the
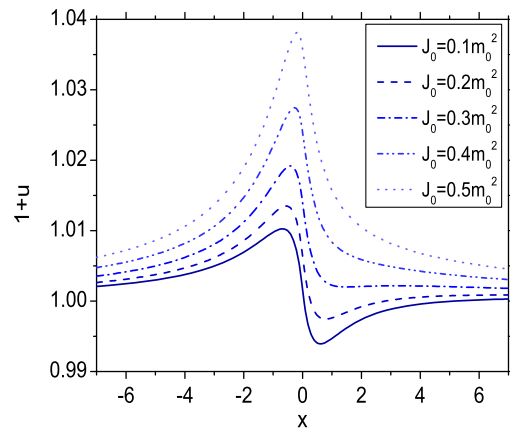

FIG. 6. The regular function $1 + u(r, \theta, \phi)$ projected onto the plane $y = z = 0$ $(\theta = 0, \phi = 0, \pi)$. We have fixed the boost parameter to $P_0 = 0.2m_0$ while varying the spin as $J_0 = 0.1m_0^2, 0.2m_0^2, .., 0.5m_0^2$ with the corresponding profiles indicated by the curves from bottom to top. We have set $N_x = 40$ and $N_y = 12$.
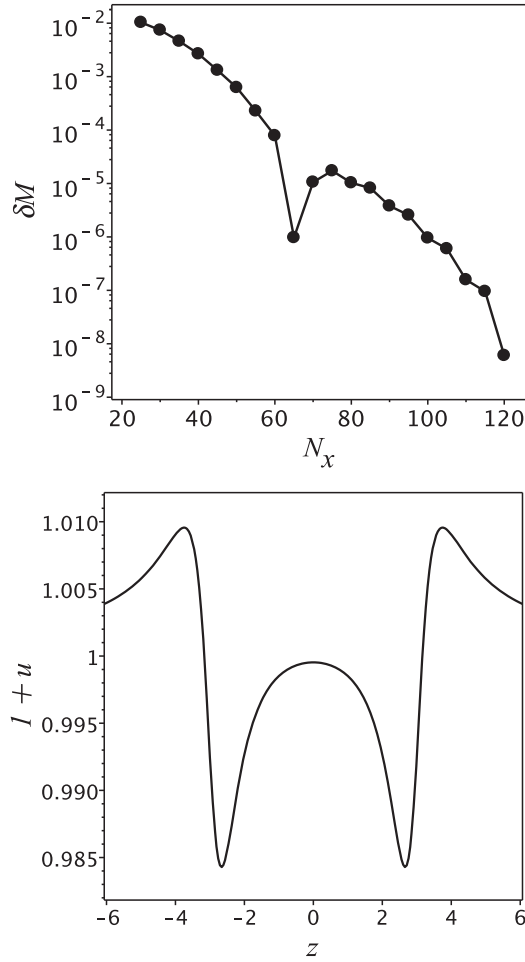
Color Scale Title

FIG. 7. Convergence of the ADM mass for the binary of boosted trumpet punctures located on the z axis with $a = 3$, $m_1 = m_2 = 0.5$, and $P_0 = 0.4m_1$. We have set $N_x = 20, 25, 30, 35, .., 100$ and $N_y = 14$. In the second panel we show the profile of $1 + u$ ($N_x = 100$, $N_y = 14$) projected onto the plane $x = y = 0$.
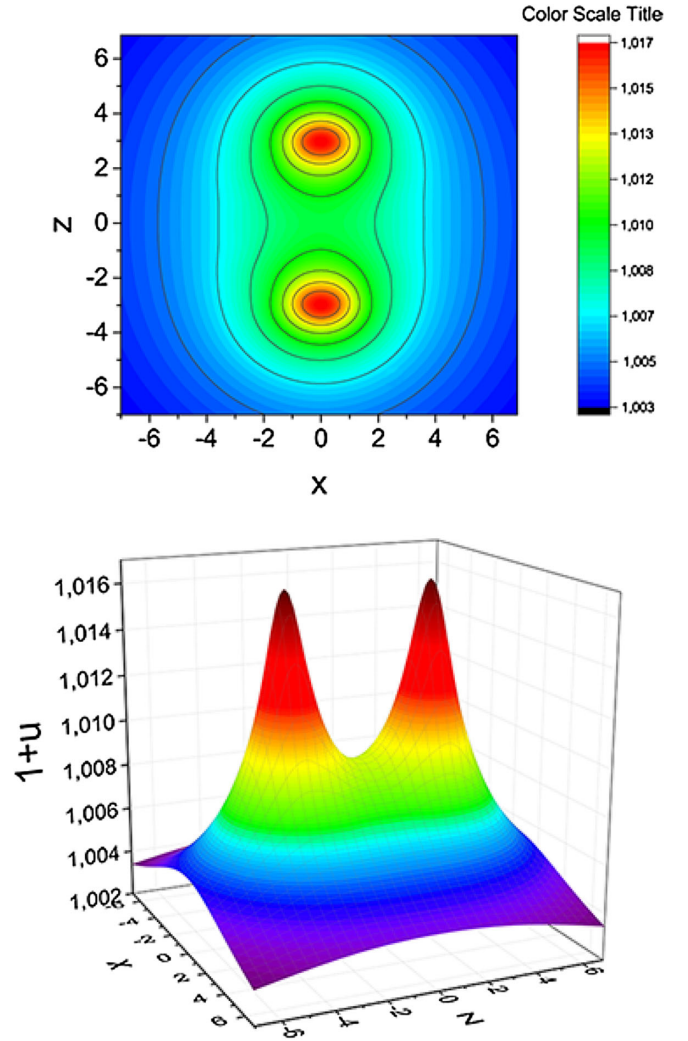
FIG. 8. Illustrations in two- and three-dimensional plots (upper and lower panels, respectively) of $1 + u$ for the binary of boosted wormhole punctures in which $a = 3$, $m_1 = m_2 = 0.5$, and $P_0 = 0.4m_1$.

regular part of the conformal factor $1 + u(r, \theta, \phi)$ can be viewed in Fig. 6, which shows the projection of $1 + u$ on the plane $y = z = 0$. Notice the deformation produced by increasing J_0 by inspecting the curves from bottom to top.

B. Binary black holes

We discuss here a boosted binary formed with trumpet punctures lying on the z axis at the coordinate locations indicated by $\mathbf{C}_1 = (0, 0, -a)$ and $\mathbf{C}_2 = (0, 0, a)$, where $2a$ is the coordinate separation between the punctures. We have adopted a simpler form of the conformal factor [24],

$$\Psi = \Psi_1 + \Psi_2 - 1 + u, \qquad (47)$$

where Ψ_1 and Ψ_2 have the same form as Ψ_0 (see Appendix A) but are centered on $\mathbf{C}_1$ and $\mathbf{C}_2$ [24], respectively. Since the momentum constraint is a linear equation, the extrinsic curvature $\bar{A}_{ij}$ is given by

$$\bar{A}_{ij} = \bar{A}_{ij}^{0(1)} + \bar{A}_{ij}^{0(2)} + \bar{A}_{ij}^{\mathbf{P}_1} + \bar{A}_{ij}^{\mathbf{P}_2}, \qquad (48)$$

and the Hamiltonian constraint becomes

$$\bar{\nabla}^2 u + \frac{1}{8}(\Psi_1 + \Psi_2 - 1 + u)^{-7}\bar{A}^{ij}\bar{A}_{ij}$$
$$- \frac{1}{8\Psi_1^7}(\bar{A}_0^{ij}\bar{A}_{ij}^0)^{(1)} - \frac{1}{8\Psi_2^7}(\bar{A}_0^{ij}\bar{A}_{ij}^0)^{(2)} = 0. \qquad (49)$$

The expression for $A_{ij}A^{ij}$ is shown in Appendix C, and $(A_{ij}^0 A_0^{ij})^{(1,2)} = 81m_{1,2}^2/r_{1,2}^6$. The algorithm presented in the last section is straightforwardly adapted to solve the Hamiltonian constraint for trumpet binary punctures with the function u approximated as indicated in Eq. (25). The radial basis function is given by Eq. (29).

To test the algorithm, we verify the convergence of the ADM mass for the axisymmetric binary system after setting $m_1 = m_2 = 0.5$, $\mathbf{P}_1 = (0, 0, P_0)$, and $\mathbf{P}_2 = (0, 0, -P_0)$,
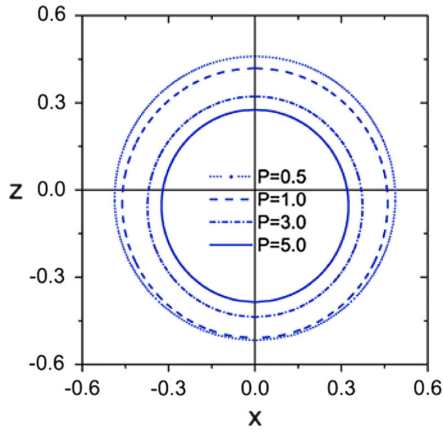
FIG. 9.   Locations of the apparent horizon $r = h(\theta)$ for a boosted black hole in the wormhole representation for several values of the momentum parameter along the z axis. The corresponding locations for the trumpet representation are similar.

together with $a = 3$ and $P_0 = 0.4m_1$. Following the convergence test, we fix $N_y = 14$, and the radial truncation order is made to vary as $N_x = 20, 25, 30, .., 100$. Figure 7 shows the exponential convergence of the ADM mass calculated according to Eq. (24) in which $m_1 + m_2$ replaces m_0. In this case, the best choice for the map parameter is the coordinate separation between the punctures, $L_0 = 2a$. For the sake of illustration we have included in Fig. 7 the plot of $1 + u(r, \theta)$ in the plane $x = y = 0$ for the binary black hole under consideration.

As the last application, we consider a three-dimensional binary formed by boosted wormhole punctures with $\mathbf{P}_1 = (P_0, 0, 0)$ and $\mathbf{P}_2 = (-P_0, 0, 0)$. The conformal factor is expressed in the same way as in Eq. (47),

$$\Psi = 1 + \frac{1}{2}\left(\frac{m_1}{r_1} + \frac{m_2}{r_2}\right) + u. \qquad (50)$$

Here the Hamiltonian constraint and the function u are given, respectively, by Eqs. (18) and (25), and the corresponding expression for $A_{ij}A^{ij}$ is given in Appendix C. The values of the parameters are the same as in Ref. [31]: $a = 3.0M$, $m_1 = m_2 = 0.5M$, and $P_0 = 0.2M$, where $M = m_1 + m_2$. In Fig. 8 we show the two- and three-dimensional plots of $1 + u(x, y = 0, z)$. We use truncation orders $N_x = 40$ and $N_y = 16$, which means 40 radial collocation points and a grid of 33×33 collocation points for the quadrature formulas given by Eq. (39).

V. FINAL REMARKS

We have presented a single-domain algorithm using the Galerkin-collocation method to solve the Hamiltonian constraint for trumpet and wormhole puncture data sets, with an emphasis on the first type of data sets. We have considered Bowen-York data including the cases of spinning, boosted, single, and binary black holes. Some features of the algorithm are worth mentioning. The spatial

domain is covered by spherical coordinates (r, θ, ϕ). In all cases, the regular part of the conformal factor is approximated by Eq. (25) with the radial basis functions satisfying the appropriate boundary conditions and taking the spherical harmonics as the angular basis functions.

To describe trumpet data corresponding to a single spinning and boosted black hole, we have proposed a puncture-like approach with a new form of the conformal factor given by Eq. (15). We have also taken into account the analytical solution that describes the trumpet Schwarzschild black hole found by Baumgarte and Naculich [21] as the background solution. This procedure is analogous to using the background solution $\Psi_0 = 1 + m_0/2r$ in the case of a single wormhole Schwarzschild black hole.

We have tested the algorithm successfully by checking the exponential convergence of the ADM mass that was present in most of the cases. In the sequence, we have made some applications of the algorithm to situations of interest. Of particular importance is the case of a single spinning trumpet black hole, in which we have shown the influence of the spin in deforming the minimal surface from a sphere to an oblate spheroid by evaluating the eccentricity of the resulting surface. The eccentricity has a limit value of about 0.439 obtained for large spin parameters. Interestingly, this value is approximately half of the eccentricity of the ergosphere of the extremal Kerr black hole.

We have revisited the radiation content present in the trumpet and wormhole single spinning and boosted black holes. In general, the radiation content is nearly the same in both families of initial data sets, as indicated by Fig. 5. We have also presented the profiles of the regular function $u(r, \theta, \phi)$ for the single trumpet black hole with spin and boost. By fixing the boost parameter P_0 and decreasing the spin J_0, we noticed that the profile approaches that of a single boosted black hole, as expected.

For the last and more illustrative applications of the algorithm, we have considered initial data for trumpet and wormhole binaries. Trumpet data consisting of binary boosted black holes was envisaged for the axisymmetric case; the ADM mass converges exponentially. For a more general case, we generated initial data with wormhole boosted black holes with the same parameters as in Ref. [31] but with truncation orders $N_x = 40$ and $N_\theta = 16$, which means 40 radial collocation points and a grid of 33×33 angular points for the quadrature formulas (39).

The Galerkin-collocation method is a viable alternative to solve the Hamiltonian constraint for the trumpet and wormhole initial data sets. We point out two directions to follow. The first is to consider $1 + \log$ trumpet data sets for which the maximal sliced conditions are relaxed [20,26]. The second is to extend the present algorithm to include more than one domain using the technique of domain decomposition.

APPENDIX A: BACKGROUND SCHWARZSCHILD TRUMPET EXACT SOLUTION

The exact expression corresponding to the maximally sliced trumpet of the Schwarzschild spacetime was derived by Baumgarte and Naculich [21]:

$$\Psi_0 = \left[\frac{4R}{2R + m_0 + \sqrt{4R^2 + 4m_0 R + 3m_0^2}}\right]^{1/2}$$
$$\times \left[\frac{8R + 6m_0 + 3\sqrt{8R^2 + 8m_0 R + 6m_0^2}}{(4 + 3\sqrt{2})(2R - 3m_0)}\right]^{1/2\sqrt{2}},$$
$$(A1)$$

where the isotropic radial coordinate r is

$$r = \left[\frac{2R + m_0 + \sqrt{4R^2 + 4m_0 R + 3m_0^2}}{4}\right]$$
$$\times \left[\frac{(4 + 3\sqrt{2})(2R - 3m_0)}{8R + 6m_0 + 3\sqrt{8R^2 + 8m_0 R + 6m_0^2}}\right]^{1/\sqrt{2}}. \quad (A2)$$

We have placed the binary punctures along the z axis $[\mathbf{C}_{1,2} = (0, 0, \pm a)]$ for the sake of convenience. The background conformal factors have the same form as Eq. (A1), however with $\Psi_1 = \Psi_1(R_1)$ and $\Psi_2 = \Psi_2(R_2)$. The relation between the areal radius R_1 and the coordinates (r, θ) is

$$\sqrt{r^2 + 2ar\cos\theta + a^2}$$
$$= \left[\frac{2R_1 + m_1 + \sqrt{4R_1^2 + 4m_1 R_1 + 3m_1^2}}{4}\right]$$
$$\times \left[\frac{(4 + 3\sqrt{2})(2R_1 - 3m_1)}{8R_1 + 6m_1 + 3\sqrt{8R_1^2 + 8m_1 R_1 + 6m_1^2}}\right]^{1/\sqrt{2}}, \quad (A3)$$

and a similar expression connecting R_2 with (r, θ).

APPENDIX B: THE APPARENT HORIZON

The apparent horizon for axisymmetric systems satisfies the following ordinary differential equation:

$$\partial_\theta^2 h = -\Gamma_{BC}^A M_A u^B u^C - \left(\frac{ds}{d\theta}\right)^2 \gamma^{\phi\phi} \Gamma_{\phi\phi}^A m_A - (\gamma^{(2)})^{-1/2}$$
$$\times \frac{ds}{d\theta} u^A u^B K_{AB} - (\gamma^{(2)})^{-1/2} \left(\frac{ds}{d\theta}\right)^3 \gamma^{\phi\phi} K_{\phi\phi}, \quad (B1)$$

where $r = h(\theta)$ describes the apparent horizon surface, $m_i = (1, -\partial_\theta h, 0)$, $u^i = (\partial_\theta h, 1, 0)$, and $(ds/d\theta)^2 = \gamma_{AB} u^A u^B$; the capital letters run over the coordinates r, θ. Since $K = 0$, it follows that $K_{ij} = A_{ij} = \Psi^2 \bar{A}_{ij}$. The conformal factor is obtained after numerically solving the Hamiltonian constraint and inserted into the apparent horizon equation.

We have introduced $\tilde{y} = \cos\theta$ and transformed the apparent horizon equation in a nonautonomous dynamical system of the type $\partial_{\tilde{y}} h = v$, $\partial_{\tilde{y}} v = f(h, v, \tilde{y})$, whose solution must satisfy the boundary conditions $\partial_\theta h = 0$ for $\theta = 0$, π or $v\sqrt{1 - \tilde{y}} = 0$ for $\tilde{y} = -1$, 1. In Fig. 9 we have shown the locations of the apparent horizon $r = h(\theta)$ for a boosted black hole using the approach described above

APPENDIX C: EXTRINSIC CURVATURE FOR BINARY BLACK HOLES

The quantity $\bar{A}_{ij} \bar{A}^{ij}$ for trumpet boosted punctures with $\mathbf{P}_1 = (0, 0, P_1)$, $\mathbf{P}_2 = (0, 0, P_2)$ and located at $\mathbf{C}_1 = (0, 0, -a)$, $\mathbf{C}_2 = (0, 0, a)$, respectively, is given by

$$\bar{A}_{ij}\bar{A}^{ij} = \frac{9P_1^2}{2r_1^6}[(1 + 2\cos^2\theta)r^2 + 6ar\cos\theta + 3a^2] + \frac{9P_2^2}{2r_2^6}[(1 + 2\cos^2\theta)r^2 - 6ar\cos\theta + 3a^2] + \frac{9P_1 P_2}{2r_1^5 r_2^5}[(1 + 2\cos^2\theta)r^6$$

$$+ (2\cos^4\theta - 14\cos^2\theta + 3)a^2 r^4 + (8\cos^2\theta + 1)a^4 r^2 - 3a^6] + \frac{81m_1^4}{8r_1^6} + \frac{81m_2^4}{8r_2^6} + \frac{81m_1^2 m_2^2}{4r_1^5 r_2^5}(2a^2 r^2\cos^2\theta + a^4 - 4a^2 r^2 + r^4)$$

$$- \frac{27\sqrt{3}m_1^2 P_1}{2r_1^6}(r\cos\theta + a) - \frac{27\sqrt{3}m_2^2 P_2}{2r_2^6}(r\cos\theta - a) - \frac{27\sqrt{3}m_2^2 P_1}{2r_1^5 r_2^5}[a^5 + a^4 r\cos\theta - 2a^3 r^2 + (2\cos^2\theta - 4)\cos\theta a^2 r^3$$

$$+ (2\cos^2\theta - 1)ar^4 + r^5\cos\theta] + \frac{27\sqrt{3}m_1^2 P_2}{2r_1^5 r_2^5}[a^5 - a^4 r\cos\theta - 2a^3 r^2$$

$$+ (-2\cos^2\theta + 4)a^2 r^3\cos\theta + (2\cos^2\theta - 1)ar^4 - r^5\cos\theta], \quad (C1)$$

where $r_1 = \sqrt{r^2 + 2ar\cos\theta + a^2}$ and $r_1 = \sqrt{r^2 - 2ar\cos\theta + a^2}$. For the case of wormhole boosted punctures located at $\mathbf{C}_1$, $\mathbf{C}_2$ with $\mathbf{P}_1 = (P_1, 0, 0)$, $\mathbf{P}_2 = (P_2, 0, 0)$, we have

$$
\bar{A}_{ij}\bar{A}^{ij} = \frac{9P_1^2}{2r_1^6}[2ar\cos\theta + a^2 + r^2 + 2r^2(1-\cos^2\theta)\cos^2\phi] + \frac{9P_2^2}{2r_2^2}(-2ar\cos\theta + a^2 + r^2 + 2r^2(1-\cos^2\theta)\cos^2\phi) + \frac{9P_1P_2}{2r_1^3r_2^3}
$$
$$
\times \left[r^2 - a^2 + \frac{2r^2(1-\cos^2\theta)(r^4 - a^4 - a^2r^2(1-\cos^2\theta))}{(2ar\cos\theta + a^2 + r^2)(r^2 - 2ar\cos\theta + a^2)}\cos^2\phi\right]. \tag{C2}
$$

[1] G. B. Cook, Living Rev. Relativ. **3**, 5 (2000).
[2] B. P. Abbott *et al.* (LIGO Scientific Collaboration and Virgo Collaboration), Phys. Rev. Lett. **116**, 061102 (2016).
[3] F. Pretorius, Phys. Rev. Lett. **95**, 121101 (2005).
[4] M. Campanelli, C. O. Lousto, P. Marroneti, and Y. Zlochower, Phys. Rev. Lett. **96**, 111102 (2006).
[5] J. G. Baker, J. Centrella, D.-I. Choi, M. Koppitz, and J. van Meter, Phys. Rev. Lett. **96**, 111102 (2006).
[6] R. Arnowitt, S. Deser, and C. W. Misner, in *Gravitation: an Introduction to Current Research*, edited by L. Witten (Wiley, New York, 1962), p. 227.
[7] J. W. York, Jr., in *Sources of Gravitational Radiation*, edited by L. L. Smarr (Cambridge University Press, Cambridge, England, 1979), p. 83.
[8] J. M. Bowen and J. W. York, Phys. Rev. D **21**, 2047 (1980).
[9] T. W. Baumgarte and S. L. Shapiro, *Numerical Relativity, Solving the Einstein's Equations on the Computer* (Cambridge University Press, Cambridge, England, 2010).
[10] S. Brandt and B. Brugmann, Phys. Rev. Lett. **78**, 3606 (1997).
[11] B. Brugmann, W. Tichy, and N. Jansen, Phys. Rev. Lett. **92**, 211101 (2004).
[12] T. W. Baumgarte, Phys. Rev. D **62**, 024018 (2000).
[13] P. Diener, F. Herrman, D. Pollney, E. Schnetter, E. Seidel, R. Takahashi, J. Thornburg, and J. Centrella, Phys. Rev. Lett. **96**, 121101 (2006).
[14] J. G. Baker, J. Centrella, D.-I. Choi, M. Koppitz, and J. R. van Meter, Phys. Rev. D **73**, 104002 (2006).
[15] J. R. van Meter, J. G. Baker, M. Koppitz, and D.-I. Choi, Phys. Rev. D **73**, 124011 (2006).
[16] T. Bode, P. Laguna, D. M. Schoemaker, I. Hinder, F. Hermann, and B. Vaishnav, Phys. Rev. D **80**, 024008 (2009).
[17] M. Hannan, S. Husa, N. O. Murchadha, B. Brugmann, J. A. Gonzalez, and U. Sperharke, J. Phys. Conf. Ser. **66**, 012047 (2007).
[18] M. Hannan, S. Husa, D. Pollney, B. Brugmann, and N. O. Murchadha, Phys. Rev. Lett. **99**, 241102 (2007).
[19] J. D. Brown, Phys. Rev. D **77**, 044018 (2008).
[20] M. Hannan, S. Husa, F. Ohme, B. Brugmann, and N. O. Murchadha, Phys. Rev. D **78**, 064020 (2008).
[21] T. W. Baumgarte and S. G. Naculich, Phys. Rev. D **75**, 067502 (2007).
[22] K. A. Denninson and T. W. Baumgarte, Classical Quantum Gravity **31**, 117001 (2014).
[23] M. Hanann, S. Husa, and N. O. Murchadha, Phys. Rev. D **80**, 124007 (2009).
[24] J. D. Immerman and T. W. Baumgarte, Phys. Rev. D **80**, 061501(R) (2009).
[25] J. P. Boyd, *Chebyshev and Fourier Spectral Methods* (Dover, New York, 2001).
[26] T. Dietrich and B. Brugmann, Phys. Rev. D **89**, 024014 (2014).
[27] H. P. de Oliveira and E. L. Rodrigues, Classical Quantum Gravity **28**, 235011 (2011).
[28] H. P. de Oliveira, E. L. Rodrigues, and J. F. E. Skea, Phys. Rev. D **84**, 044007 (2011).
[29] H. P. de Oliveira and E. L. Rodrigues, Phys. Rev. D **86**, 064007 (2012).
[30] H. P. Pfeiffer, L. E. Kidder, M. A. Scheel, and S. Teukolsky, Comput. Phys. Commun. **152**, 253 (2003).
[31] M. Ansorg, B. Brugmann, and W. Tichy, Phys. Rev. D **70**, 064011 (2004).
[32] M. Ansorg, Classical Quantum Gravity **24**, S1 (2007).
[33] S. Ossokine, F. Foucart, H. P. Pfeiffer, M. Boyle, and B. Szilagyi, Classical Quantum Gravity **32**, 245010 (2015).
[34] B. A. Finlayson, *The Method of Weighted Residuals and Variational Principles* (Academic Press, New York, 1972).
[35] B. Fornberg, *A Pratical Guide to Pseudospectral Methods* (Cambridge University Press, Cambridge, England, 1998).
[36] G. B. Cook, Ph.D. thesis, University of North Carolina at Chapel Hill, 1990.
[37] G. B. Cook and J. W. York, Phys. Rev. D **41**, 1077 (1990).
[38] D. Christodoulou, Phys. Rev. Lett. **25**, 1596 (1970).